Single-ion tracks in $Gd_2Zr_{2-x}Ti_xO_7$ pyrochlores irradiated with swift heavy ions

Maik Lang,[1] Jie Lian,[2] Jiaming Zhang,[1] Fuxiang Zhang,[1] William J. Weber,[3] Christina Trautmann,[4] and Rodney C. Ewing[1,*]
[1]*Department of Geological Sciences and Department of Materials Science and Engineering, University of Michigan, Ann Arbor, Michigan 48109, USA*
[2]*Department of Mechanical, Aerospace, and Nuclear Engineering, Rensselaer Polytechnic Institute, Troy, New York 12180, USA*
[3]*Pacific Northwest National Laboratory, Richland, Washington 99352, USA*
[4]*GSI Helmholtzzentrum für Schwerionenforschung, 64291 Darmstadt, Germany*
(Received 11 December 2008; published 4 June 2009)

Swift xenon ions (1.43 GeV) were used to systematically investigate the radiation response of pyrochlores in the $Gd_2Zr_{2-x}Ti_xO_7$ binary in the electronic energy loss regime. Ion-induced structural modifications were characterized by synchrotron x-ray diffraction, Raman spectroscopy, and transmission electron microscopy. The structure of ion tracks depends on the pyrochlore composition, and the damage cross section increases with the Ti content. In general, single ion tracks consist of an amorphous track core, surrounded by a crystalline, but disordered, defect-fluorite-structured shell. That is in turn surrounded by a defect-rich pyrochlore region. The decrease in the size of these different track zones, with increasing Zr content, is a result of the enhanced radiation stability of Zr-rich pyrochlore within individual swift heavy ion tracks.

DOI: 10.1103/PhysRevB.79.224105 PACS number(s): 61.80.−x, 61.05.cp, 61.82.Ms, 64.60.Cn

I. INTRODUCTION

The pyrochlore structure, with the ideal formula of $A_2B_2O_7$, exhibits a remarkable range of composition, with over 500 different combinations of *A*- and *B*-site cations having been synthesized.[1,2] The *A*-site cation is generally occupied by larger tri- and tetravalent actinides and lanthanides, and the *B* site is typically Ti, Zr, Hf, or Sn. This structural flexibility, with inherent oxygen vacancies, leads to a wide spectrum of physical, chemical, and electrical properties that are important in a number of technological applications.[1] Recently, there has been increased interest in using materials with fluorite and fluorite-related structures, such as pyrochlore, as potential host phases for the immobilization of actinides.[3–10] Radiation damage from alpha-decay events of the incorporated actinides can cause structural changes, such as macroscopic swelling, and a decrease in the chemical durability of the nuclear waste form,[11] which may deteriorate its long-term performance. Remarkably, the pyrochlore structure displays a wide range of responses to irradiation, which are mainly determined by its chemical composition and bond type.[12–15]

The structure of pyrochlore is isometric ($Fd\bar{3}m$, $Z=8$, and $a=0.9-1.2$ nm) and is closely related to the ideal fluorite structure (AX_2), except that there are two cation sites and one-eighth fewer anions. The anion "vacancies" are ordered on the anion sublattice. The *A*-site cation is eight coordinated and located within a distorted cubic coordination polyhedron; whereas, the *B*-site cation is six coordinated and located within a distorted octahedron.[1,2] The stability of the pyrochlore structure strongly depends on the radius ratio of the *A*- and *B*-site cations, r_A/r_B,[16] which are included in Table I for the $Gd_2Zr_{2-x}Ti_xO_7$ binary. If this ratio exceeds 1.78, the ordered pyrochlore structure is no longer the stable phase for $A_2B_2O_7$ materials, and the monoclinic structure will form. If the radius ratio drops below 1.46, a disordered, defect-fluorite structure forms in which the *A*- and *B*-type cations are randomly distributed over the *A* and *B* sites, and the oxygen vacancies are disordered on the anion sublattice. The transformation from the ordered pyrochlore to the disordered, defect-fluorite structure is energetically favored as r_A/r_B decreases. Besides this compositionally driven order-disorder transformation, thermal treatment[17] and the application of high pressure[18] can cause the pyrochlore-to-fluorite transformation. In addition, the disordering of some pyrochlores can be induced by ion-beam irradiation.[19,20]

Due to its potential use as a host structure for the immobilization of actinides, many studies[13,19,21–26] have simulated the α-decay damage from incorporated actinides in a wide variety of pyrochlore compositions using ion-beam irradiations in the energy range of keV–MeV, where elastic collisions with the target atoms dominate the damage process (nuclear energy loss). These systematic studies have demonstrated, particularly in the systems $A_2Ti_2O_7$ and $A_2Zr_2O_7$,[9,10,13,19,21–23] the importance of structure, bond-type, and electronic configuration on the radiation stability of pyrochlore. The interpretation of the experimental results has been further explored by computational simulations of the energetics of the disordering process.[27,28] In the $Gd_2Zr_{2-x}Ti_xO_7$ binary, the radiation-induced amorphization is the dominant process for Ti-rich pyrochlores; whereas, an order-disorder transformation to the defect-fluorite structure is the main result for Zr-rich pyrochlores.[12–15,29] The resistance to ion-beam-induced amorphization increases dramatically with zirconium content,[12] and the end-member pyrochlore $Gd_2Zr_2O_7$ remains crystalline at doses as high as ~100 dpa when exposed at room temperature to 200 keV Ti ions.[23] This radiation resistance is a result of an increased stability of the defect-fluorite structure as the radius ratio of the *A*- and *B*-site cations, r_A/r_B, decreases. However, as recently demonstrated, the only means to substantially amorphize $Gd_2Zr_2O_7$ are by MeV C_{60}-cluster projectiles, which deposit extremely high energy densities.[30]

This study concentrates on irradiation with swift heavy ions in the GeV energy range, which simulates the fission products released by either spontaneous fission, such as observed in $Gd_2Ti_2O_7$ containing ^{244}Cm,[11] or neutron-induced

TABLE I. Summary of track diameters for all pyrochlore compositions. The TEM values were directly obtained from bright-field images [error represents sigma of 20 individual measurements (Fig. 1)]. Diameters from XRD and Raman spectroscopy were deduced from cross sections (Figs. 4 and 6) by assuming cylinder geometry of modified volume. The errors result from the corresponding fitting procedures. The results are graphically illustrated in Fig. 7(a).

Pyrochlore $Gd_2Zr_{2-x}Ti_xO_7$ (x)	Cation radius ratio r_A/r_B	Synchrotron XRD d (nm)	Bright-field TEM d (nm)	Raman spectroscopy d (nm)
2	1.74	4.6 ± 0.7	9.2 ± 0.9	11.4 ± 1.2
1.5	1.66	4.1 ± 0.4	6.8 ± 0.6	9.0 ± 0.6
1	1.59	3.6 ± 0.2	5.4 ± 0.4	7.7 ± 0.5
0.5	1.52	2.1 ± 0.1	4.6 ± 0.7	6.1 ± 0.5
0	1.46	0	3.5 ± 0.4	4.6 ± 0.6

fission for inert matrix nuclear fuel applications. Such projectiles slow down in matter predominantly by interactions with the target electrons inducing excitations and ionizations along the ion path. The energy is first spread among the electrons and is finally transferred to the atomic structure. In many solids (predominantly in insulators), cylindrical damage zones, the so-called ion "tracks" are created if the energy deposition to the atoms is sufficiently high.[31] Track formation typically occurs above a critical energy loss (dE/dx) threshold, which is material dependent.[32] Examples of material modifications are crystalline-to-amorphous[33] or superconductor-to-insulator[34] transformations, the creation of a high-temperature[35] or high-pressure phase,[36] generation of defect clusters,[37] and enormous irreversible deformations.[38–40] For the mechanism of ion-track creation, different models, such as Coulomb explosion and thermal spike, have been proposed,[41,42] but no consistent theory has been established that fully describes all aspects of the track-formation process. For a given target material, track formation depends primarily on dE/dx and ion velocity.[31] Many ion-beam studies have investigated the size and morphology of tracks in detail, and different approaches have been applied to deduce the cross section of the damage under consideration. Structural modifications can be studied by direct imaging [e.g., transmission electron microscopy (TEM)] or indirect analysis [e.g., Raman spectroscopy and x-ray diffraction (XRD)].

This paper is a detailed characterization of single ion tracks in $Gd_2Zr_{2-x}Ti_xO_7$ pyrochlores irradiated with 1.43 GeV Xe ions. Earlier irradiation experiments with swift heavy ions in the MeV-GeV energy regime have focused on the accumulated material modifications of different pyrochlores.[29,30,43,44] The final structural modification of the $Gd_2Zr_{2-x}Ti_xO_7$ binary at high irradiation fluences strongly depends on the Ti and Zr content.[29] Similar to the effects of low-energy irradiations, swift heavy projectiles induce primarily amorphization in Ti-rich pyrochlore and create the fully disordered, defect-fluorite structure in Zr-rich pyrochlore.[29] By the combination of various analytical methods, including TEM, synchrotron XRD, and Raman spectroscopy, the present study provides insights into the nature and geometry of phase transitions that occur within a single ion track. Details of the damage cross sections and track characteristics for the different pyrochlores were analyzed, and overall track diameters including the dimensions of different structure domains were determined as a function of pyrochlore composition.

II. EXPERIMENTAL PROCEDURE

Polycrystalline samples of the $Gd_2Zr_{2-x}Ti_xO_7$ binary were used for $x=0$, 0.5, 1, 1.5, and 2. The starting materials were dense pellets with a typical grain size on the order of a few μm. The calculated density ranged from 6.64 g/cm^3 ($Gd_2Zr_2O_7$) to 6.56 g/cm^3 ($Gd_2Ti_2O_7$). The mm-thick samples were polished (roughness: ≤ 1 μm) without specific orientation down to a thickness of ~ 40 μm and subsequently annealed at 800 °C for 24 h to release absorbed water. For irradiation, the pellets were cut into small pieces, ~ 0.25 cm^2. The ion-irradiation experiments were performed at the beamline X0 of the UNILAC linear accelerator at the GSI (Helmholtzzentrum für Schwerionenforschung) in Darmstadt, Germany using 1.43 GeV ^{129}Xe ions at room temperature and under normal incidence. The irradiation flux was limited to $\sim 10^8$ ions/cm^2·s, which is low enough to avoid significant sample heating. The projected range of the projectiles is approximately 55 μm[45] and, thus, 15 μm greater than the sample thickness. The ions completely passed through the sample depositing an almost constant electronic energy loss of 28.5 ± 1.5 keV/nm (the dE/dx variation within a given sample is less than 5%).[45] This estimate was used for all pyrochlore compositions because their density differences, and thereby differences in electronic stopping powers, are insignificant. The nuclear energy loss is neglected because it is about 3 orders of magnitude lower than the electronic energy loss. Nine sets of samples were prepared and irradiated to fluences (Φ) between 1×10^{10} and 1×10^{13} ions/cm^2 with an absolute accuracy of 10%–20%. Since the different pyrochlores for a given fluence were irradiated simultaneously and the fluence series was performed with the same beam settings, the relative error should be even less.

The irradiated samples were characterized by TEM with a JEOL 2010F instrument providing both bright-field and high-resolution images, as well as electron diffraction patterns. Samples for TEM examination were prepared by crushing the irradiated crystals into a fine powder subsequently deposited onto a holey-carbon TEM grid. The irradiation of the TEM samples was limited to $\Phi \leq 1 \times 10^{11}$ ions/cm^2 in order to image nonoverlapping, individual ion tracks.

Angle-dispersive synchrotron powder XRD measurements were performed at the beamline B2 of the Cornell High Energy Synchrotron Source (CHESS) of Cornell University. A monoenergetic beam of 25 keV (λ=0.496 Å), with spot size of ~1 mm^2, was used in transmission mode to analyze ion-induced structural modifications throughout the entire sample. The measuring times were optimized to gain maximum intensity and, thus, varied from sample to sample. Debye diffraction rings were recorded with a mar345 image plate detector, and the integrated two-dimensional patterns were produced with the software FIT2D.[46] In order to compare data from different samples, the intensity of each pattern was normalized to the same (strongest) diffraction maximum. The amorphous fraction of each sample was deduced by deconvoluting the XRD patterns into individual crystalline and amorphous contributions and subsequent peak fitting (details of this procedure are described in an earlier study[29]).

Raman spectra were recorded in backscattering geometry using a HORIBA Jobin Yvon (HR800) micro-Raman spectrometer with a 20 mW HeNe-laser as excitation source (λ =632.82 nm). The Raman signal was collected from a spot diameter of ~2 μm on the polished sample surface. The measuring times varied from sample to sample and were optimized to gain maximum intensity similar to the XRD measurements. In order to compare the data of different samples, the intensity of each spectrum was normalized to the same (strongest) vibration mode. The Raman data were analyzed for ion-induced intensity reductions of the vibration modes with the HORIBA Jobin Yvon software package LABSPEC.

III. RESULTS

A. Single track microstructure

The irradiated, crushed grains for the TEM analysis were randomly oriented; thus, the tracks could be imaged in all orientations (e.g., perpendicular to or along their length). Bright-field TEM images are shown in Fig. 1 where the tracks are clearly visible due to their different contrast with respect to the surrounding matrix. The track contrast is most pronounced for Ti-rich compositions [$Gd_2Ti_2O_7$, Fig. 1(a)] and becomes weaker and smaller in size with increasing Zr content [see Figs. 1(a)–1(c)]. Starting with the Zr-rich composition $Gd_2Zr_{1.5}Ti_{0.5}O_7$, the tracks show some contrast variation along their length, which may be an indication for the onset of a discontinuity in the radiation damage along the ion path [Fig. 1(c)]. The weakest tracks were observed for the gadolinium zirconate end member (not shown here) for which the contrast was so weak that the tracks were almost not visible. The size of the tracks in the different pyrochlores was measured by visually estimating the position of the parallel boundaries between the modified contrast and the unchanged matrix for tracks with a large aspect ratio [e.g., Fig. 1(b)]. Except for $Gd_2Zr_2O_7$, about 20 tracks were analyzed for each composition; their mean values and the standard deviations are summarized in Table I. The diameter data for $Gd_2Zr_2O_7$ are only an estimate based on a few tracks because a reliable measurement was difficult due to the very weak track contrast. The TEM analysis reveals that the mean track

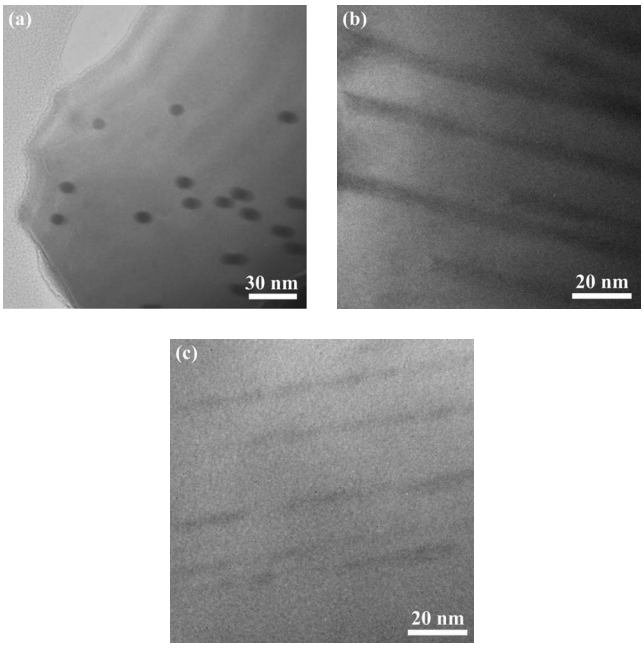

FIG. 1. Bright-field TEM images of three different pyrochlore compositions after irradiation with 1.43 GeV Xe ions of fluence 1×10^{11} ions/cm^2. The individual damage trails are evident by the contrast variation in (a) top view as well as in [(b) and (c)] cross-sectional view. The size and contrast are at a maximum for tracks in (a) $Gd_2Ti_2O_7$ and decrease systematically for (b) Gd_2ZrTiO_7 and (c) $Gd_2Zr_{1.5}Ti_{0.5}O_7$.

diameter, *d*, increases systematically with the Ti content of the pyrochlore, and the diameter of tracks in $Gd_2Ti_2O_7$ is on average more than a factor of 2 larger than those in $Gd_2Zr_2O_7$.

The detailed track structure was analyzed by high-resolution TEM images (Fig. 2). Tracks in $Gd_2Ti_2O_7$ consist of an amorphous core (width: 3–4 nm) surrounded by a ~2 nm broad track zone of the defect-fluorite structure [Fig. 2(a)]. The disordered crystalline phase in this region has the same crystallographic orientation as the surrounding pyrochlore matrix. The dark contrast at the interface between the defect-fluorite and the pyrochlore structure is most likely caused by strain due to the relative volume changes within the different phases (amorphous, defect fluorite, and pyrochlore). In the immediate vicinity of the fluorite-structured track region, some weaker contrast variations, extending to 3–4 nm into the surrounding pyrochlore matrix, probably originate from simple point defects and associated residual strain. The amorphous-fluorite and the fluorite-pyrochlore structure boundaries are relatively sharp; however, in the cross-section image [Fig. 2(b)] some variations along the length of the track are visible. A very similar track structure, consisting of different damage zones, was also found for the Ti-rich pyrochlore composition $Gd_2Zr_{0.5}Ti_{1.5}O_7$ [Fig. 2(c)], however, with less sharp boundaries between the different zones and less pronounced structural modifications. With increasing Zr content, individual tracks are increasingly less distinct in the high-resolution TEM images, which is consistent with the weaker track contrast in the bright-field images [e.g., Fig. 1(c)]. For $Gd_2Zr_{1.5}Ti_{0.5}O_7$ [Fig. 2(d)], the different

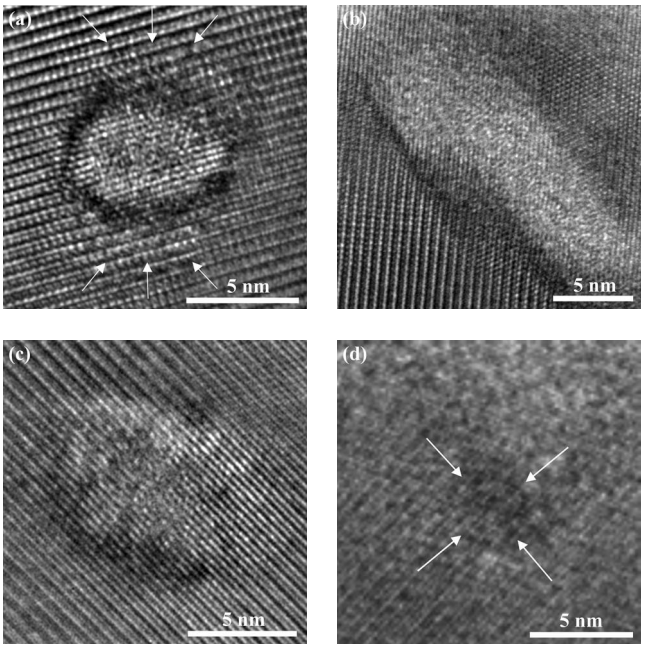

FIG. 2. High-resolution TEM images of [(a) and (b)] $Gd_2Ti_2O_7$, (c) $Gd_2Zr_{0.5}Ti_{1.5}O_7$, and (d) $Gd_2Zr_{1.5}Ti_{0.5}O_7$ after irradiation with 1.43 GeV Xe ions of fluence 1×10^{11} ions/cm^2. (a) Top view image clearly shows that an individual ion track in gadolinium titanate consists of an amorphous core (~3–4 nm) and a disordered, defect-fluorite-structured shell (~2 nm). Weak contrast variations (see arrows) can be attributed to a defect-rich pyrochlore halo. (b) Cross-section image reveals the fluctuations in the boundary between the amorphous domain and the still crystalline, but disordered, domain. (c) The track structure is similar for the Ti-rich composition, but the damages zones are less pronounced. (d) In the Zr-rich composition no amorphization is evident and the different contrast in the pyrochlore matrix (see arrows) is caused by the strain induced by the formation of the defect-fluorite structure.

damage zones could no longer be detected within the tracks, and structural changes are only evident by weak circular contrast modifications in the pyrochlore matrix (see arrows). Fast Fourier transform (FFT) analysis confirms that these tracks consist primarily of the disordered, defect-fluorite structure; no amorphization was evident in the TEM analysis for this composition or for the zirconate end-member $Gd_2Zr_2O_7$.

B. Amorphous phase characterization

Synchrotron XRD was used to obtain structural details of the pyrochlore before and after irradiation. Figure 3(a) shows the XRD patterns of the Ti-rich composition $Gd_2Zr_{0.5}Ti_{1.5}O_7$ for various fluences. The assignments of the diffraction maxima are given for the spectra of the unirradiated sample. The unirradiated material consists of the ordered pyrochlore structure, evident by the pronounced diffraction maxima of the pyrochlore superstructure (e.g., 111 diffraction maximum at $2\theta\sim5°$). Upon irradiation, the intensities of all sharp crystalline diffraction maxima are reduced, and the diffuse scattering of the amorphous phase becomes apparent at $2\theta\sim9$ and $2\theta=12-18°$. The ion-induced amorphization increases

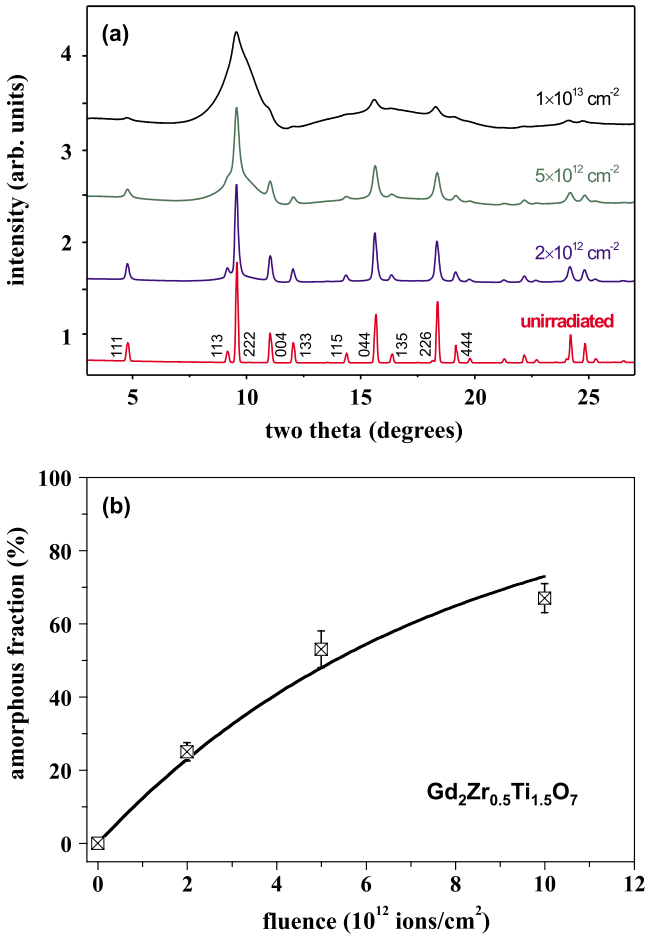

FIG. 3. (Color online) (a) Synchrotron XRD patterns of $Gd_2Zr_{0.5}Ti_{1.5}O_7$ before and after irradiation with 1.43 GeV Xe ions of increasing ion fluence (bottom to top). The diffuse scattering of the amorphous phase is evident for higher fluences by the increased background. (b) The amorphous fraction, as revealed by quantitative analysis of (a) XRD patterns as a function of irradiation fluence. The curve represents the fit of Eq. (1) to the data points, and the errors are from the determination of the amorphous fraction (Ref. 29).

with fluence, but full amorphization is not achieved for this composition even at the maximum fluence of 1×10^{13} ions/cm^2, which is consistent with previous TEM results for samples in this series irradiated to the same fluence.[29] For quantitative analysis, the contributions of the crystalline and amorphous phases were deduced by a deconvolution procedure with subsequent peak fitting.[29] As a function of fluence, the amorphous fraction [Fig. 3(b)] grows linearly in the initial stage and finally begins to saturate at higher fluences. This evolution is described by an exponential equation based on a direct-impact model,[47]

$$A(\Phi) = A_0(1 - e^{-(\sigma\cdot\Phi)}), \tag{1}$$

where A represents the amorphous fraction, σ is the amorphization cross section per incident ion, and Φ is the ion fluence. The constant A_0 gives the maximum achievable amorphization and was set to 100% when fitting Eq. (1) to the data [Fig. 3(b)] since all the Ti-rich pyrochlores ($x=1$,

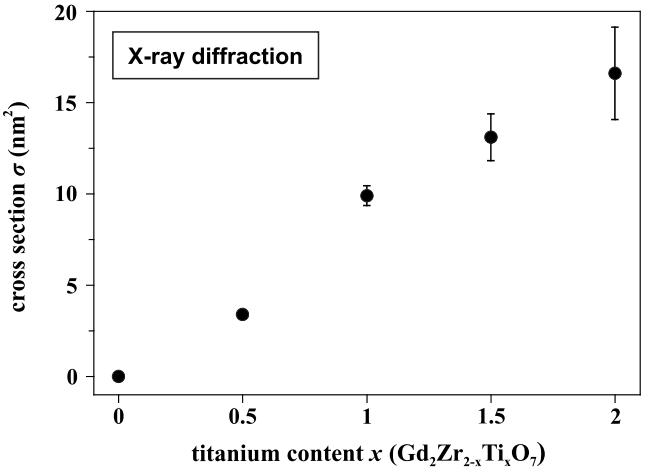

FIG. 4. Cross section, σ, of amorphization process for all pyrochlores as a function of composition (Ti content). The cross sections were obtained by fitting Eq. (1) to the XRD data. The errors represent the uncertainty of the fitting processes.

1.5, and 2) readily amorphize at room temperature under irradiation with both low-energy heavy ions[13,14] and swift heavy ions.[29] In the direct-impact model, amorphization is described by the accumulation of individual amorphous tracks (linear increase up to about 3×10^{12} ions/cm^2). At larger fluences, tracks begin to overlap, and the increase in amorphous fraction becomes sublinear. Finally, amorphization evolves toward a plateau for substantial track overlap [not yet reached in Fig. 3(b)]. Fitting Eq. (1) to the XRD data of all compositions allowed for the estimate of the amorphization cross section, σ, and the corresponding effective track diameter, d, of the amorphous track zone by assuming cylindrical track symmetry ($\sigma=\pi(d/2)^2$). Both σ (Fig. 4) and d (Table I) increase systematically with increasing Ti content, indicating that the Xe ions amorphize the Ti-rich pyrochlores more efficiently than Zr-rich compositions. This finding is consistent with an earlier XRD study,[29] including Rietveld refinements, which demonstrated that Zr-rich pyrochlores are predominately transformed to the disordered, defect-fluorite structure, and ion-induced amorphization occurs to a much lesser extent.

C. Characterization of vibrational modes

Repeated Raman measurements at different locations on the surface of polished polycrystalline samples showed no orientation effects, demonstrating that the different crystals do not affect the Raman intensities of any of the peaks. The measuring time was adjusted to maximize the Raman signal, and for better comparison, all spectra were normalized to the strongest vibration mode. Ion-induced structural modifications and their expression in the Raman spectra are discussed for the Ti-rich composition $Gd_2Zr_{0.5}Ti_{1.5}O_7$ [Fig. 5(a)]. Based on previous work,[14,15] the most prominent Raman band at 310 cm^{-1} can be assigned to the O-Gd-O bending mode. With increasing fluence, the intensity of this crystalline vibration mode decreases while simultaneously a new broad peaklike structure appears at ~750 cm^{-1} [Fig. 5(a)],

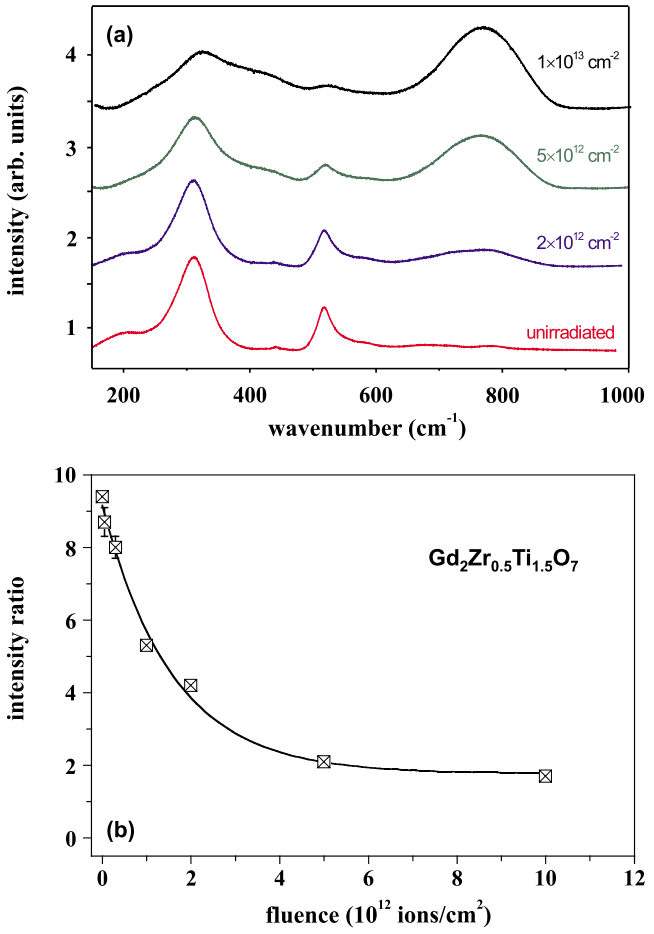

FIG. 5. (Color online) (a) Raman spectra of $Gd_2Zr_{0.5}Ti_{1.5}O_7$ before and after irradiation with 1.43 GeV Xe ions with increasing ion fluence (bottom to top). The intensity of the O-Gd-O bending mode (~310 cm^{-1}) decreases substantially, which is accompanied by the growth of a new broad peak from the amorphous volume (~750 cm^{-1}). (b) Intensity of the ~310 cm^{-1} peak normalized to the intensity of the spectral region at ~470 cm^{-1} as a function of irradiation fluence. The curve represents the fit of Eq. (2) to the data points, and the error bars reflect the uncertainties from the determination of the peak-intensity ratio.

which is ascribed to amorphous domains.[48] For the highest fluence, 1×10^{13} ions/cm^2, the broad band of the amorphous volume clearly dominates the spectrum, but remnants of the crystalline fraction are still evident. With increasing fluence, the overall background becomes very high; therefore, it was not possible to deduce reliable quantitative data on the amorphous fraction by an analysis of the peak area, similar to that applied to the XRD data. Instead, the intensity ratio of the strongest maximum at 310 cm^{-1} to the minimum of the neighboring spectral region (450–500 cm^{-1}) was analyzed. This ratio strongly decreases with fluence [Fig. 5(b)], which is due to a loss of crystallinity and concomitant amorphization [Fig. 5(a)]. Furthermore, the transition from the ordered pyrochlore to the disordered, defect-fluorite structure is accompanied by an intensity decrease of the O-Gd-O bending mode.[49] Other modifications in the pyrochlore structure, such as strain-induced distortion of bonds and simple defects (e.g., point defects), additionally contribute to the intensity

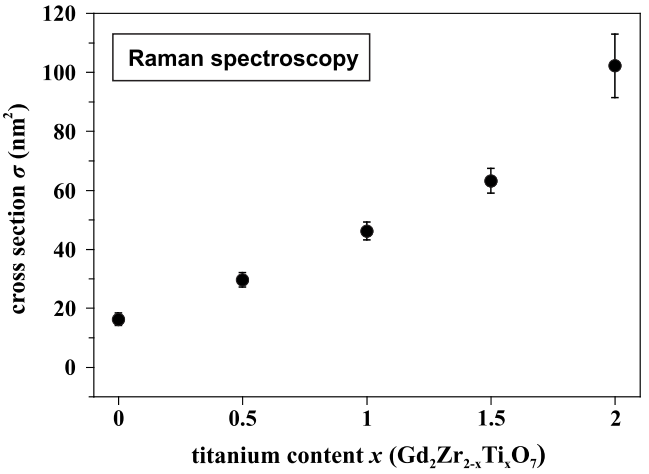

FIG. 6. Cross section, σ, of the intensity decrease of the O-Gd-O bending mode ($\sim$310 cm^{-1}) as a function of pyrochlore composition (Ti content). The cross sections were obtained by fitting Eq. (2) to Raman data, and the errors represent the uncertainty of the fitting processes.

reduction.[50] The exponential decrease in the intensity ratio as function of irradiation fluence [Fig. 5(b)] can be well described by the following equation, similar to that used in an earlier XRD and Raman investigation:[50]

$$I(\Phi) = a + be^{-(\sigma\cdot\Phi)}, \tag{2}$$

where I represents the peak-intensity ratio at a given fluence, Φ, and σ denotes the damage cross section per incident ion. The constant, a, is the minimum intensity ratio, and b is a fit parameter. Both a and b are dependent on material characteristics (e.g., composition and microstructure) and irradiation conditions (e.g., temperature). By fitting Eq. (2) to the present Raman data, σ is deduced for all pyrochlore compositions (Fig. 6). Similar to the XRD data (Fig. 4), the cross section increases systematically with the Ti content, but the absolute value deduced from Raman spectroscopy is larger for any given composition. The effective track diameter, d, was obtained for all compositions from the cross section, assuming cylindrical symmetry (Table I). It should be noted that a in the limit of very large Φ should approach values of around 1.0 (with the crystalline O-Gd-O bending modes becoming indistinguishable from the background minimum). The small offset observable in Fig. 5(b) was of similar size for all compositions and is primarily caused by the asymmetric background (higher intensity at lower wavenumbers); however, some residual O-Gd-O bending modes may also remain due to the stochastic nature of the short-range order in the amorphous state.

IV. DISCUSSION

A combination of several complementary analytical techniques has been used to investigate beam-induced modifications in the pyrochlore binary: $Gd_2Zr_{2-x}Ti_xO_7$. The different probes have been used to ascertain the size of individual ion tracks by either direct measurements (TEM) or, indirectly, from cross-section data obtained from fitting fluence-dependent expressions to the data (XRD and Raman spectroscopy). For a given composition, each analytical technique produces different track diameters because they probe different length scales of the material (Fig. 7; Table I); however, all diameters increase systematically with increasing Ti content. TEM and Raman spectroscopy reveal a very similar linear trend with increasing Ti content [lines with nearly identical slopes in Fig. 7(a)]; whereas, the XRD data exhibit a linear dependence on d^2, or cross-sectional area, as shown more clearly in Fig. 7(b). This linear dependence of the track cross section on Ti content may indicate the strong role of local energy-deposition density in determining the amorphous core diameter.

The track diameters obtained by synchrotron XRD are the smallest among the three techniques. The damage cross section per incident ion was determined by the increasing amorphous background in the XRD patterns [Fig. 3(a)], without considering other types of radiation-damage contributions (e.g., the formation of zones of the disordered, defect-fluorite structure). Thus, the corresponding track diameter represents the effective diameter of the amorphous core within the track, as produced by each incident ion. This interpretation is strongly supported by the "zero" track diameter (i.e., no amorphous background detected in the XRD pattern) for the zirconate end member, $Gd_2Zr_2O_7$ (Fig. 7) and is consistent with the fact that amorphization has never been reported for irradiations of the material with monatomic ions.[13–15,29,30,44]

The mean track diameter, as measured by TEM, corresponds to the width of the cylinder according to contrast variations along the ion trajectory (Fig. 1). In particular, for Ti-rich compositions, it was evident that both the amorphous material and the disordered, defect-fluorite structures contribute to this contrast change [Figs. 2(a)–2(c)]. Therefore, the diameter associated with the bright-field TEM analysis represents a track size that includes both types of radiation-damage states (amorphous+defect-fluorite). This explains the larger diameters, as compared with the results from the XRD measurements [Fig. 7(a)].

Raman spectroscopy yields information on the overall damage related to the intensity decrease of the O-Gd-O bending mode (Fig. 5). This decrease is partly induced by the loss of crystallinity (i.e., increase in amorphous phase[29]) but also contains contributions from the order-to-disorder transformation from the pyrochlore to the defect-fluorite structure.[49] Finally, defects in the pyrochlore structure (e.g., interstitials, vacancies, or other simple defects) and strain-induced distortion of the ⟨Gd-O⟩ bonds also contribute to this intensity decrease.[50] The track diameters obtained by Raman spectroscopy therefore reflect the total contribution from all the radiation-damage states (amorphous+defect-fluorite +defects and strain), which results in the largest diameter values [Fig. 7(a)].

The results show that different analytical probes are sensitive to different types of structural modifications in a track due to different effective damage cross sections. This is in agreement with earlier radiation-damage studies in other materials.[51–54] The combination of techniques provides a semiquantitative track description consisting of concentric cylindrical zones. Except for $Gd_2Zr_2O_7$, where there is no amorphization, a swift heavy ion track in the $Gd_2Zr_{2-x}Ti_xO_7$

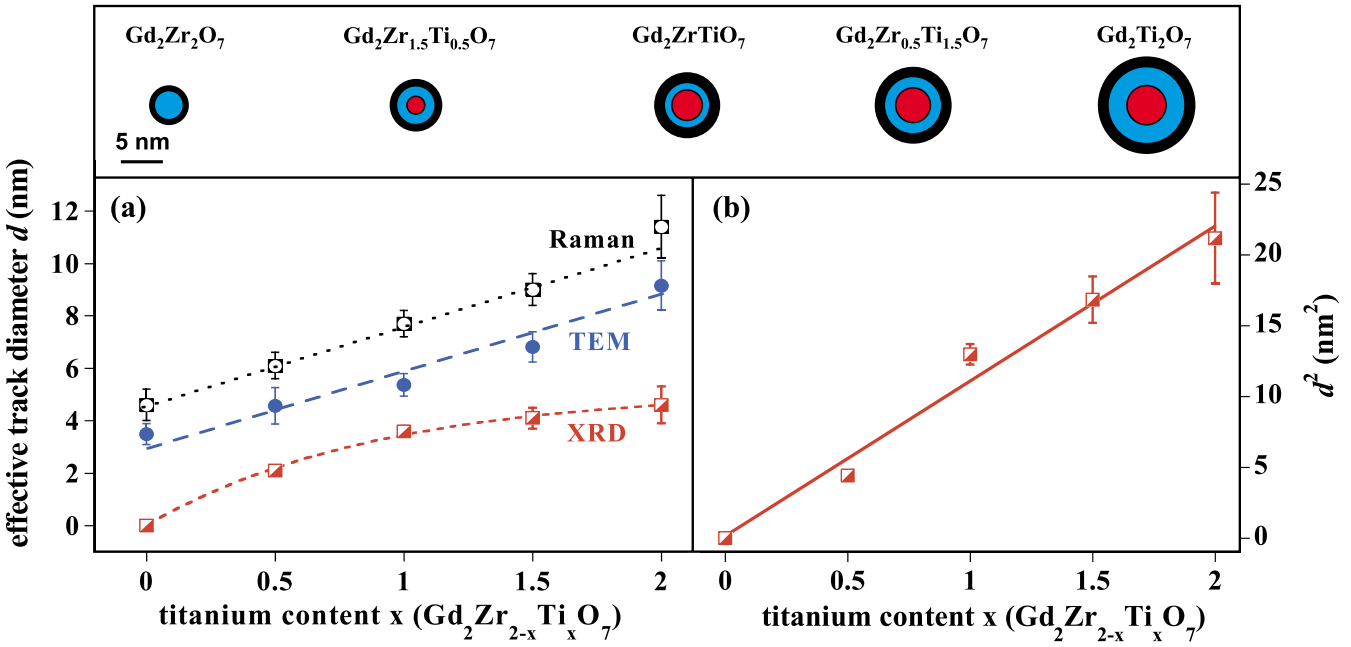

FIG. 7. (Color online) Track diameter as a function of pyrochlore composition (Ti content). The mean diameter values and uncertainties for XRD and Raman spectroscopy were obtained from the corresponding damage cross sections (Figs. 4 and 6). The diameters from TEM analysis were directly measured from bright-field images (Fig. 1), and the errors represent sigma of 20 individual measurements. The inset illustrates schematically the concentric track cylinders (amorphous core, disordered defect-fluorite-structured shell, and strained defect-rich pyrochlore halo) for all pyrochlore compositions.

binary has an *amorphous core*, surrounded by a *disordered, defect-fluorite-structured shell* and a *strained, defect-rich pyrochlore halo* (schematically illustrated by concentric circles of the inset in Fig. 7). For the Ti end member, $Gd_2Ti_2O_7$, the damage morphology and size of individual damage zones are in general agreement with the actual track structure as imaged by high-resolution TEM [Fig. 2(a)]. Both the amorphous core and the surrounding disordered, defect-fluorite-structured shell are clearly evident in the single ion track. Individual point defects in the defect-rich, pyrochlore halo are not revealed by TEM; however, some contrast modifications are evident in the pyrochlore matrix that surrounds the defect-fluorite structure. For other pyrochlores, the individual damage zones were too weak and small to be clearly observed in high-resolution TEM images.

The occurrence of different track zones, which was also observed in other investigations,[55,56] can be explained by the specifics of ion-solid interactions in the electronic energy loss regime. A purely energetic approach describes the different damage zones qualitatively as a direct consequence of the energy-deposition process. In the center of the track, the energy deposition is at its maximum value and decreases with increasing distance, r, from the ion trajectory with $\sim 1/r^2$.[57] The strong reduction in the energy density with increasing distance from the track center is directly related to the degree of radiation damage observed within the different zones. The most severe damage, the amorphous domain, is induced within the core of the track due to the peak energy deposition and exhibits a dependence on local energy density (d^2). In the track shell region, amorphization is no longer achieved, and the dominant radiation response is a transformation from the ordered pyrochlore to the disordered, defect-fluorite structure. At even greater distances from the track core, in the track halo, the deposited energy is only sufficient to create individual point defects in the pyrochlore matrix. Thus, there are two critical energy density thresholds that have to be overcome during the energy deposition in order to produce either amorphous domains or the disordered, defect fluorite. Since the energy density depends on the beam conditions (i.e., ion species and energy), irradiations at different electronic energy losses and/or ion velocities should contribute to understanding the nature and size of the individual damage zones.

A more detailed description of ion-track formation can be obtained by the inelastic thermal-spike model, which explains radiation damage quantitatively as a result of quenching of a molten phase that is created along the ion path.[42,58] In this model, the ion energy is first deposited to the electron subsystem and subsequently transferred to the atoms via electron-phonon coupling. Thermal diffusion between the two subsystems is described by coupled differential equations. According to this model, track formation is governed by the thermal parameters, including thermal conductivity, melting temperature, and heat of fusion. The different damage zones within a track can be attributed to radial temperature variations and related quenching kinetics. For a detailed description, however, it is essential to distinguish directly induced modifications (e.g., defect-fluorite shell formed at reduced peak temperature) from recovery/annealing effects subsequent to the quenching process (e.g., defect-fluorite shell as the recrystallization product of the amorphous phase). Irradiations at different temperatures combined with the complex track structure of $Gd_2Zr_{2-x}Ti_xO_7$ pyrochlores provide an ideal system to systematically study annealing effects related to the thermal-spike model.

The schematic illustration of the different track regions (inset of Fig. 7) represents a rather idealized picture and does not consider discontinuous track morphology as evidenced for Zr-rich compositions [Fig. 1(c)]. However, it is very useful when comparing the radiation-damage characteristics for the different pyrochlore compositions. The size of each damage zone in the schematic illustration is to scale for all five examples (inset of Fig. 7). The corresponding core, shell, and halo radii become larger with increasing Ti content, and the overall track diameter for the Ti end member is about 2.5 times larger than the Zr end member. This observation may be related to the thermal properties of the different pyrochlore compositions and thermal-spike effects induced by swift heavy ions. The melting temperature of $Gd_2Zr_2O_7$ is ~2550 °C,[59] which is higher than that for $Gd_2Ti_2O_7$, which is ~1800 °C.[60] Although the melting temperatures for the intermediate compositions of the $Gd_2Zr_{2-x}Ti_xO_7$ binary are not presently available, it can be assumed that the melting temperature should systematically decrease with increasing Ti content. The larger track diameters for pyrochlores of higher Ti content [Fig. 7(a)] are probably a direct consequence of the reduced melting temperature, resulting in a larger molten track zone controlled by the density of energy deposition. For a more detailed description of the track size and character dependence on Ti content, systematic thermal-spike calculations are required, but these will require more details on materials properties, such as thermal conductivity.

In addition to thermal-spike effects, structural changes in different pyrochlores (variation in radius ratio r_A/r_B) and correlated thermodynamic properties[16] may contribute to the modifications in track size and morphology with composition. Consistent with the reduced radiation stability for Ti-rich compositions reported earlier,[13–15,29,44] the overall track size significantly increases with the Ti content. This could be attributed to instantaneous recrystallization processes and enhanced defect annealing with increasing Zr content, which could also explain the reduction in diameter of the defect-fluorite domains and amorphous core in such compositions. The nearly constant incremental diameter difference between the TEM and Raman diameters as a function of Ti content is related to a dependence on a constant radial rate of change for all compositions, such as heat loss or the radial velocity of the order-disorder transformation, but more detailed analysis and simulations are needed to confirm the details of this process.

V. CONCLUSIONS

Radiation damage in pyrochlores of the $Gd_2Zr_{2-x}Ti_xO_7$ binary induced by 1.43 GeV Xe ions has been systematically investigated using three complementary analytical techniques: synchrotron XRD, Raman spectroscopy, and TEM. By combining the different techniques, single tracks were shown to consist of three distinct concentric damage zones: (1) an amorphous track core, (2) a shell of the disordered, defect-fluorite structure, and (3) a distant halo of defect-rich pyrochlore. The complex variation in structure reflects the nonlinear radial dose deposition of a swift heavy ion. These structural variations within a single track are very similar to macroscopic phase transformations observed in the overlapping fluence regime described in earlier ion-beam studies.[13–15,29,44] The composition of pyrochlore has a strong effect on the details of the ion-beam-induced structural changes. In Ti-rich pyrochlore, amorphization is the dominant process; whereas, for Zr-rich compositions, the disordered, defect-fluorite structure is the dominant radiation-damage structure. Remarkably, the radiation resistance significantly increases with the Zr content, which is evident in the steady increase in the overall damage (total track diameter) with decreasing Zr content due to the substitution of Ti.

ACKNOWLEDGMENTS

The authors gratefully acknowledge technical support during the irradiation by the Materials Research Group of GSI and for the sample preparation by James Hinchcliff at the University of Michigan. This work was supported by the Office of Basic Energy Sciences, U.S. Department of Energy through Grant No. DE-FG02-97ER45656 at UM and under Contract No. DE-AC05-76RL01830 at PNNL. The use of CHESS beam is supported by the NSF and NIH/NIGMS via NSF Grant No. DMR-0225180. M.L. acknowledges support from the German Science Foundation DFG.

*Corresponding author; rodewing@umich.edu

[1] M. A. Subramanian, G. Aravamudan, and G. V. S. Rao, Prog. Solid State Chem. **15**, 55 (1983).
[2] B. C. Chakoumakos, J. Solid State Chem. **53**, 120 (1984).
[3] K. E. Sickafus, L. Minervini, R. W. Grimes, J. A. Valdez, M. Ishimaru, F. Li, K. J. McClellan, and T. Hartmann, Science **289**, 748 (2000).
[4] R. C. Ewing, W. J. Weber, and J. Lian, J. Appl. Phys. **95**, 5949 (2004).
[5] W. J. Weber and T. R. C. Ewing, Science **289**, 2051 (2000).
[6] W. J. Weber and R. C. Ewing, in *Scientific Basis for Nuclear Waste Management XXV*, MRS Symposia Proceedings No. 713 (Materials Research Society, Warrendale, 2002), p. 443.
[7] K. B. Helean, A. Navrotsky, E. R. Vance, M. L. Carter, B. Ebbinghaus, O. Krikorian, J. Lian, L. M. Wang, and J. G. Catalano, J. Nucl. Mater. **303**, 226 (2002).
[8] A. A. Digeos, J. A. Valdez, K. E. Sickafus, S. Atio, R. W. Grimes, and A. R. Boccaccini, J. Mater. Sci. **38**, 1597 (2003).
[9] P. E. Raison and R. G. Haire, Prog. Nucl. Energy **38**, 251 (2001).
[10] S. S. Shoup, C. E. Bamberger, and R. G. Haire, J. Am. Ceram. Soc. **79**, 1489 (1996).
[11] W. J. Weber, J. W. Wald, and H. Matzke, Mater. Lett. **3**, 173 (1985).
[12] S. X. Wang, L. M. Wang, R. C. Ewing, and K. V. G. Kutty, in *Microstructural Processes in Irradiated Materials*, MRS Sym-

posia Proceedings No. 540 (Materials Research Society, Warrendale, 1999), p. 355.
[13] S. X. Wang, B. D. Begg, L. M. Wang, R. C. Ewing, W. J. Weber, and K. V. G. Kutty, J. Mater. Res. **14**, 4470 (1999).
[14] B. D. Begg, N. J. Hess, D. E. McCready, S. Thevuthasan, and W. J. Weber, J. Nucl. Mater. **289**, 188 (2001).
[15] N. J. Hess, B. D. Begg, S. D. Conradson, D. E. McCready, P. L. Gassmann, and W. J. Weber, J. Phys. Chem. B **106**, 4663 (2002).
[16] J. Lian, K. B. Helean, B. J. Kennedy, L. M. Wang, A. Navrotsky, and R. C. Ewing, J. Phys. Chem. B **110**, 2343 (2006).
[17] B. J. Wuensch, K. W. Eberman, C. Heremans, E. M. Ku, P. Onnerud, E. M. Yeo, S. M. Haile, J. K. Stalick, and J. D. Jorgensen, Solid State Ionics **129**, 111 (2000).
[18] F. X. Zhang, J. W. Wang, J. Lian, M. K. Lang, U. Becker, and R. C. Ewing, Phys. Rev. Lett. **100**, 045503 (2008).
[19] S. X. Wang, L. M. Wang, R. C. Ewing, G. S. Was, and G. R. Lumpkin, Nucl. Instrum. Methods Phys. Res. B **148**, 704 (1999).
[20] J. Lian, L. Wang, J. Chen, K. Sun, R. C. Ewing, J. M. Farmer, and L. A. Boatner, Acta Mater. **51**, 1493 (2003).
[21] B. D. Begg, N. J. Hess, W. J. Weber, R. Devanathan, J. P. Icenhower, S. Thevuthasan, and B. P. McGrail, J. Nucl. Mater. **288**, 208 (2001).
[22] J. Lian, L. M. Wang, R. C. Ewing, and L. A. Boatner, Nucl. Instrum. Methods Phys. Res. B **241**, 365 (2005).
[23] J. Lian, X. T. Zu, K. V. G. Kutty, J. Chen, L. M. Wang, and R. C. Ewing, Phys. Rev. B **66**, 054108 (2002).
[24] J. Lian, J. Chen, L. M. Wang, R. C. Ewing, J. M. Farmer, L. A. Boatner, and K. B. Helean, Phys. Rev. B **68**, 134107 (2003).
[25] J. Lian, R. C. Ewing, L. M. Wang, and K. B. Helean, J. Mater. Res. **19**, 1575 (2004).
[26] J. Lian, L. M. Wang, R. G. Haire, K. B. Helean, and R. C. Ewing, Nucl. Instrum. Methods Phys. Res. B **218**, 236 (2004).
[27] W. R. Panero, L. P. Stixrude, and R. C. Ewing, Phys. Rev. B **70**, 054110 (2004).
[28] J. W. Wang, F. X. Zhang, J. Lian, R. C Ewing, and U. Becker (to be published).
[29] M. Lang, F. X. Zhang, J. Lian, C. Trautmann, Z. Wang, and R. C. Ewing, J. Mater. Res. **24**, 1322 (2009).
[30] J. Zhang, M. Lang, J. Lian, J. Liu, C. Trautmann, S. Della-Negra, M. Toulemonde, and R. C. Ewing, J. Appl. Phys. **105**, 113510 (2009).
[31] *Ion Beam Science: Solved and Unsolved Problems*, edited by M. Toulemonde, W. Assmann, C. Dufour, A. Meftah, F. Studer, C. Trautmann, and P. Sigmund (The Royal Danish Academy of Sciences and Letters, Copenhagen, 2006), pp. 263–292.
[32] J. Liu, R. Neumann, C. Trautmann, and C. Müller, Phys. Rev. B **64**, 184115 (2001).
[33] A. Meftah, F. Brisard, J. M. Constantini, E. Dooryhee, M. Hage-Ali, M. Hervieu, J. P. Stoquert, F. Studer, and M. Toulemonde, Phys. Rev. B **49**, 12457 (1994).
[34] H. Walter, W. Prusseit, R. Semerad, H. Kinder, W. Assmann, H. Huber, H. Burkhardt, D. Rainer, and J. A. Sauls, Phys. Rev. Lett. **80**, 3598 (1998).
[35] W. Assmann, M. Dobler, D. K. Avasthi, S. Kruijer, H. D. Mieskes, and H. Nolte, Nucl. Instrum. Methods Phys. Res. B **146**, 271 (1998).
[36] H. Dammak, A. Barbu, A. Dunlop, D. Lesueur, and N. Lorenzelli, Philos. Mag. Lett. **67**, 253 (1993).
[37] K. Schwartz, C. Trautmann, and R. Neumann, Nucl. Instrum. Methods Phys. Res. B **209**, 73 (2003).
[38] S. Klaumünzer, L. Changlin, S. Löffler, M. Rammensee, and G. Schumacher, Nucl. Instrum. Methods Phys. Res. B **39**, 665 (1989).
[39] A. Hedler, S. Klaumünzer, and W. Wesch, Nature Mater. **3**, 804 (2004).
[40] C. Trautmann, S. Klaumünzer, and H. Trinkaus, Phys. Rev. Lett. **85**, 3648 (2000).
[41] H. Trinkaus and A. I. Ryazanov, Phys. Rev. Lett. **74**, 5072 (1995).
[42] M. Toulemonde, Ch. Dufour, A. Meftah, and E. Paumier, Nucl. Instrum. Methods Phys. Res. B **166-167**, 903 (2000).
[43] M. K. Patel, V. Vijayakumar, D. K. Avasthi, S. Kailas, J. C. Pivin, V. Grover, B. P. Mandal, and A. K. Tyagi, Nucl. Instrum. Methods Phys. Res. B **266**, 2898 (2008).
[44] G. Sattonnay, S. Moll, L. Thomé, C. Legros, M. Herbst-Ghysel, F. Garrido, J.-M. Costantini, and C. Trautmann, Nucl. Instrum. Methods Phys. Res. B **266**, 3043 (2008).
[45] SRIM, 2006, http://www.srim.org/SRIM/SRIM2006.htm
[46] A. P. Hammersley, *FIT2D* (ESRF, Grenoble, France, 1998).
[47] W. J. Weber, Nucl. Instrum. Methods Phys. Res. B **166-167**, 98 (2000).
[48] F. X. Zhang, B. Manoun, S. K. Saxena, and C. S. Zha, Appl. Phys. Lett. **86**, 181906 (2005).
[49] D. Michel, M. Perez, Y. Jorba, and R. Collongues, J. Raman Spectrosc. **5**, 163 (1976).
[50] W. J. Weber and N. J. Hess, Nucl. Instrum. Methods Phys. Res. B **80-81**, 1245 (1993).
[51] M. Toulemonde and F. Studer, Philos. Mag. A **58**, 799 (1988).
[52] J. M. Costantini, F. Ravel, F. Brisard, M. Caput, and C. Cluzeau, Nucl. Instrum. Methods Phys. Res. B **80-81**, 1249 (1993).
[53] R. Neumann, Nucl. Instrum. Methods Phys. Res. B **151**, 42 (1999).
[54] M. Boccanfuso, A. Benyagoub, K. Schwartz, C. Trautmann, and M. Toulemonde, Nucl. Instrum. Methods Phys. Res. B **191**, 301 (2002).
[55] K. Schwartz, C. Trautmann, T. Steckenreiter, O. Geiß, and M. Krämer, Phys. Rev. B **58**, 11232(9) (1998).
[56] S. Abu Saleh and Y. Eyal, Nucl. Instrum. Methods Phys. Res. B **209**, 113 (2003).
[57] R. Katz, K. S. Loh, L. Daling, and G.-R. Huang, Radiat. Eff. Defects Solids **114**, 15 (1990).
[58] A. Meftah, J. M. Costantini, N. Khalfaoui, S. Boudjadar, J. P. Stoquert, F. Studer, and M. Toulemonde, Nucl. Instrum. Methods Phys. Res. B **237**, 563 (2005).
[59] A. G. Karaulov, E. I. Zoz, and T. M. Shlyakhova, Refract. Ind. Ceram. **37**, 83 (1996).
[60] J. Chen, J. Lian, L. M. Wang, R. C. Ewing, J. Matt Farmer, and L. A. Boatner, in *Scientific Basis for Nuclear Waste Management XXV*, MRS Symposia Proceedings No. 713 (Materials Research Society, Warrendale, 1998), p. 501.